Carbon 129 (2018) 476–485

Contents lists available at ScienceDirect

Carbon

journal homepage: www.elsevier.com/locate/carbon

Characterization of ultralow thermal conductivity in anisotropic pyrolytic carbon coating for thermal management applications

Yuzhou Wang [a], David H. Hurley [b], Erik P. Luther [c], Miles F. Beaux II [c], Douglas R. Vodnik [c], Reuben J. Peterson [c], Bryan L. Bennett [c], Igor O. Usov [c], Pengyu Yuan [d], Xinwei Wang [d], Marat Khafizov [a, *]

[a] Department of Mechanical and Aerospace Engineering, Nuclear Engineering Program, The Ohio State University, Columbus, OH, 43210, USA
[b] Idaho National Laboratory, P.O. Box 1625, Idaho Falls, ID, 83415, USA
[c] Los Alamos National Laboratory, P.O. Box 1663, Los Alamos, NM, 87545, USA
[d] Department of Mechanical Engineering, Iowa State University, Ames, IA, 50011-2161, USA

ARTICLE INFO

Article history:
Received 9 August 2017
Received in revised form
8 December 2017
Accepted 10 December 2017
Available online 11 December 2017

ABSTRACT

Pyrolytic carbon (PyC) is an important material used in many applications including thermal management of electronic devices and structural stability of ceramic composites. Accurate measurement of physical properties of structures containing textured PyC layers with few-micrometer thickness poses new challenges. Here a laser-based thermoreflectance technique is used to measure thermal conductivity in a 30-μm-thick textured PyC layer deposited using chemical vapor deposition on the surface of spherical zirconia particles. Raman spectroscopy is used to confirm the graphitic nature and characterize microstructure of the deposited layer. Room temperature radial and circumferential thermal conductivities are found to be 0.28 W m^{-1} K^{-1} and 11.5 W m^{-1} K^{-1}, corresponding to cross-plane and in-plane conductivities of graphite. While the anisotropic ratio of the in-plane to cross-plane conductivities is smaller than previous results, the magnitude of the smallest conductivity is noticeably smaller than previously reported values for carbon materials and offers opportunities in thermal management applications. Very low in-plane and cross-plane thermal conductivities are attributed to strong grain boundary scattering, high defect concentration, and small inter-laminar porosity. Experimental results agree with the prediction of thermal transport model informed by the microstructure information revealed by Raman spectroscopy.

1. Introduction

For over five decades pyrolytic carbon (PyC) has been used in many technological applications ranging from structural composites to biomedical devices. It is an allotrope of carbon structurally identical to graphite having a hexagonal intra-plane structure and weak inter-plane bonding [1,2]. The difference in the in-plane and out-of-plane bonding can lead to very strong anisotropic thermal and electrical properties. Major differences between graphite and PyC stem from their origin. Graphite is derived from natural sources or fabricated by heating petroleum coke, a carbonaceous solid resulting from oil refining, at temperatures above 2000 °C. On the other hand, PyC is fabricated using chemical vapor deposition (CVD) or chemical vapor infiltration (CVI) techniques [3,4]. The grains in graphite are typically randomly oriented resulting in isotropic properties on a long range, whereas the CVD process allows deposition of textured layers. There are a number of experimental methods used to characterize and quantify the texture of PyC including optical ellipsometry, electron diffraction, and polarized Raman spectroscopy [5–8]. Depending on the approach, PyC is generally categorized into different groups with decreasing structural order: high texture, medium texture, low texture and isotropic [6]. Another classification considers the texture on a different scale with categories: rough laminar, smooth laminar, and isotropic [9]. Highly ordered pyrolytic graphite (HOPG) belongs to the first group and granular isotropic PyC to the last.

Oftentimes PyC is used in composite materials. In polymer composites, addition of small PyC fibers have been shown to improve their thermal performance [10,11]. Ceramic matrix fiber

* Corresponding author.
E-mail address: Khafizov.1@osu.edu (M. Khafizov).

https://doi.org/10.1016/j.carbon.2017.12.041
0008-6223/

composites of silicon carbide utilize PyC as an interphase layer between the fiber and the matrix to act as a barrier to crack propagation through fibers [12]. In nuclear applications, tri-structural isotropic (TRISO) fuel contains several layers of PyC to improve its structural integrity and fission retention [13,14]. For the majority of applications, it is preferred to employ the isotropic form of PyC with randomly oriented polycrystallites to overcome issues with directional aging, anisotropic expansion, and swelling [15].

The in-plane and out-of-plane thermal conductivity for highly ordered PyC (also called HOPG) are 2000 and 6.8 W m^{-1} K^{-1}, respectively, and these values differ by two orders of magnitude [1,2,16]. This strong thermal anisotropy makes PyC a promising material for new directional heat management applications. For example, in electronic devices, textured PyC can act as a heat spreader or insulator depending on the direction.

A particular application that can exploit PyC's low conductivity is enhancing the performance of self-regulating heaters and protection of electronic devices from overheating. These devices employ positive temperature coefficient of resistivity, where in the event of an overheating the active element's resistivity increases, decreasing the current and thus resulting in the reduction of Joule heating. The low thermal conductivity of the thermal barrier coating applied around the heater would make this feedback mechanism more efficient by trapping the heat early during a transient, and resulting in a more prompt response to prevent irreversible damage to the device.

Current practical application of the PyC as a thermal barrier coating is envisioned in nuclear fission reactors. Here a rapid increase of the neutron flux and associated heat generation during a reactivity insertion is regulated by nuclear fuel's negative temperature reactivity coefficient [17]. PyC used as a thermal barrier coating around the fuel particle allows one to take advantage of the reactivity feedback more efficiently in order to achieve improved control of the nuclear reactor. PyC is particularly attractive here due to its compatible physical, chemical and nuclear properties with the environment present in nuclear applications [18].

Another potential application not necessarily related to thermal management is the use of the ultra-low thermal conductivity PyC as a thermoelectric device where heat is directly converted to electricity. With the chemical intercalation applied to graphite to drastically increase the population of electrons and holes, graphite has become an effective thermoelectric material [19]. The low conductivity could contribute to the increase of Seebeck coefficient, key parameter for the efficiency of thermoelectric generators.

In light of these applications, accurate measurement of anisotropic thermal conductivity in as-fabricated structures becomes increasingly important to fully utilizing PyC in new thermal management schemes. A fair amount of work has been done to measure microstructural anisotropy with micron scale resolution [5,6,20]. However, fewer experiments have been conducted to measure the anisotropic thermal conductivity in micron size structures such as nuclear fuel particles or microelectronic assemblies [21].

Traditional methods to measure thermal conductivity of graphite and other carbon allotropes include the steady state heat flux method, laser flash, and Raman scattering microscopy [16,22–24]. The first two methods require large, centimeter sized, specially designed samples and provide values averaged over a few millimeter scale. As a result these two methods are not suitable for studies requiring micron-scale spatial resolution [24–26]. The Raman method is typically used in the measurement of thermal transport in low-dimensional systems such as one-dimensional carbon nanotubes and two-dimensional materials including graphene and its variants [22,23,27,28]. Additional benefit of Raman spectroscopy is the ability to characterize disorder and anisotropy of PyC [29]. Laser-based thermoreflectance microscopy has emerged as a powerful method for nondestructively measuring thermal properties with a micron-scale spatial resolution [30–35]. Additionally, important for this study, it offers a capability to measure anisotropic thermal conductivity that a standard implementation of the Raman thermometry lacks [36–38]. Thermoreflectance approach is based on the optical measurement of thermally induced changes of optical reflectivity [39]. This technique has been successfully applied to characterize carbon fibers and irradiated ceramics [21,40,41]. Our investigation combining both Raman spectroscopy and thermoreflectance methods further explores the possibility of these approaches to provide an attractive toolbox to study the impact of microstructure on thermal transport in ceramic materials [42].

In this work, we use spatially resolved modulated thermoreflectance microscopy to measure the anisotropic thermal conductivity in a thin PyC layer surrounding a spherical particle [33,34,43]. This particle is part of a surrogate nuclear fuel sample, where the low thermal conductivity coating is a novel design feature providing a method to impede the heat flow from the fuel particle to the graphite matrix during power transients. This allows to raise fuel temperature and take advantage of the negative reactivity feedback due to Doppler broadening to reduce thermal power during a reactivity transient. This self-regulating feature of the fuel can be employed in nuclear thermal propulsion and advanced power reactors. It is thus important to precisely measure the thermal properties of individual layers of this particle, especially conductivity in the radial direction.

The remainder of the paper is structured as follows. First we review the details of experimental methods in section 2. Experimental results including microstructure characterization of the PyC layer, the modulated thermoreflectance measurements, and Raman thermography are presented in section 3. In section 4, a continuum heat diffusion model used to determine the thermal conductivity tensor components is introduced. Section 5 describes the analysis of the experimental results to determine thermal conductivity. Lastly, a discussion of the experimentally measured conductivities within the framework of thermal transport model is presented.

2. Experimental methods

2.1. Sample fabrication

The PyC layer was deposited using a fluidized bed CVD method [44]. The texture of the PyC layer is influenced by deposition conditions including gas flow rate and composition, temperature, and substrate [3]. To achieve desired texture, temperature was kept between 1130 and 1170 °C and gas flow rate was set to 1200 sccm for both methane (CH_4) and argone (Ar) gas. Approximately 30 μm thick PyC coatings were deposited on the surface of 5% yttria stabilized zirconia (YSZ) spherical particles. The coated spherical particles were mixed with a graphite powder and a binder, compacted, and heat treated for 1 h at 950 °C. Additional details of sample fabrication will be available in the forthcoming publication [45]. Produced compact was sliced into a thin disc using a wire diamond saw and mechanically polished. Raman spectroscopy and thermography were applied on an as-polished sample, while for the thermoreflectance measurements, a few nanometer thick gold layer was sputter coated on the surface after the polishing step.

2.2. Modulated thermoreflectance approach

Modulated thermoreflectance (MTR) method was used to investigate thermal transport in radial and circumferential directions of the PyC layer [39,43,46]. In this method, a thin metallic layer is deposited on the surface of the sample to ensure strong

optical absorption and good temperature transduction. One beam (pump) serves as a heat source. The intensity of the pump is modulated using either a sinusoidal or square wave profile. The second laser beam (probe) monitors small temperature induced changes in the reflectivity of the metal layer.

The pump and probe beams were derived from two continuous wave diode lasers emitting at 660 nm and 532 nm wavelength, respectively. Amplitude modulation of the pump was achieved by direct modulation of the laser output via electronic trigger. Both pump and probe were focused on the sample using a single 50 × microscope objective resulting in a spot size of ~1 μm for each beam. Lateral scanning was achieved through an optical two lens lever [46]. Small changes in reflectivity of the probe beam ΔR/R ranging from 10^{-5} to 10^{-3} were measured using the lock-in amplification of a voltage signal generated in the photodiode upon excitation by the incident probe beam. The frequency of the pump was tuned from 1 kHz to 100 kHz to ensure good sensitivity to the thermal properties of the substrate [43]. Spatially resolved amplitude and phase profiles of the thermal wave were measured by recording reflectivity changes of the probe beam while the pump was laterally scanned on the surface of the sample.

2.3. Raman thermometry

Uncoated PyC sample was irradiated by a continuous wave 532 nm green laser using a 50× objective lens. The Raman signals of the sample were collected by a confocal Raman system (Voyage, B&W Tek, Inc.) with a spectral resolution of 2 cm^{-1}. The position of the PyC sample is controlled by a 3-D nano-stage. The excitation energy is adjusted by a variable ND filter. The laser beam size on the sample is 0.68 μm which is 1/e radius of the laser intensity profile.

Raman thermometry (RT) was used as an alternative method for measuring thermal conductivity [22]. The thermal conductivity measurement is based on the temperature dependence of Raman bands located at 1350 cm^{-1} (D-band) and 1580 cm^{-1} (G-band) at ambient conditions. Steady state temperature at the center of the excitation beam was determined from the position of the peaks. Temperature dependence on the incident power was analyzed to determine the thermal conductivity. This approach applied to anisotropic system allows the determination of only one independent parameter, making it insufficient on its own, but in this case, it served as a validation of MTR results.

In the Raman temperature calibration experiments, the PyC sample is placed on a heated stage and a voltage transformer that powers the heater, and the sample's surface temperature is monitored by a thermocouple. We also completed Raman scanning for the measurement area of 20 × 20 μm^2. The variation in Raman intensity is only 3.2% which indicates the experiment area is very uniform.

3. Experimental results

Fig. 1(top right) shows an SEM image of a cross-sectional view of one of the particles. The brighter region corresponds to the YSZ spherical particle coated with the thin PyC layer (dark gray). Concentric rings appearing within the PyC layer suggest a laminar structure with some porosity or debonding between layers. A two-modulator generalized ellipsometer was used to verify the anisotropic texture of the PyC layer [20]. The diattenuation coefficient was found to be $N = 0.21$, which can be contrasted to $N = 0.59$ for highly textured HOPG and $N = 0$ for an isotropic material [47]. Based on the texture classification of similarly fabricated layers, these results indicate that the deposited PyC layer exhibits highly textured structure [48].

In our implementation, spatially resolved amplitude and phase profiles of the thermal wave were measured by recording the reflectivity changes of the probe beam located at the center of the PyC layer while the pump was laterally scanned across the probe beam along radial and circumferential directions of the spherical particle [37]. To simplify our analysis, we chose the largest particle for thermal transport measurements. Limiting the scan distance to be much smaller than the radius of curvature of the particle enables us to neglect effects associated with the curvature. Measured phase profiles along radial and circumferential directions of the spherical shell over a 1 kHz - 100 kHz frequency range are shown in Fig. 2. This range corresponds to the frequencies whose profiles have a good signal to noise ratio and provide sensitivity to the thermal properties of the PyC layer. In the central region, the phase is affected by the finite spot size of the pump laser. Outside this region the relation between phase and scan distance is linear with a slope that is related to the diffusion length of the wave which is proportional to an effective diffusivity of the layered system [43,46]. When two different materials are measured under similar conditions, the material that exhibits a steeper slope in the phase profile in general has a smaller thermal diffusivity. This is especially valid in the low frequency limit where the thermal wave profiles are most sensitive to the diffusivity of the substrate material [46,49].

The difference in the slopes of phase profiles measured along radial and circumferential directions are noticeable as can be seen in Fig. 2. The difference is largest for the low frequency response (1 kHz) and barely noticeable at the highest frequency (100 kHz). These results suggest an anisotropic thermal conductivity in the PyC layer. Because the slopes in the radial direction are larger, we can qualitatively conclude that thermal conductivity along the radial direction is smaller than along the circumferential direction. In general, our observation is consistent with previous reports where spatially resolved measurements were applied to demonstrate anisotropic conductivity in quartz single crystal, silicon nitride and PyC layer [37,38,50].

Additionally, we performed separate measurements on the YSZ spherical particle and a Pyrex glass slide. The results of these and PyC measurements can be represented using an alternative approach that only captures the information contained in slopes of the linear portions of the measured thermal wave profiles. Fig. 3 shows an effective diffusivity as a function of frequency for 4 different sets of thermal wave profiles corresponding to radial and circumferential directions of PyC, isotropic YSZ and isotropic Pyrex. The effective diffusivity that includes contribution from the metallic film layer was calculated using the following procedure: first the linear portions of the profiles were fitted to determine the slope, then this slope was used to define an effective diffusivity using $D_e = \pi f/\text{slope}^2$, where f is the modulation frequency of the pump.

Fig. 3 suggests that diffusivity of PyC in the radial/circumferential direction is smaller/larger than those of Pyrex and YSZ. Considering that both YSZ and Pyrex have conductivity values in the range of 1–2 W m^{-1} K^{-1}, we anticipate conductivity of PyC in the radial direction to be smaller than 1 W m^{-1} K^{-1}. The interpretation of D_e in PyC is further complicated by its anisotropic nature. As a result, quantitative determination of the conductivity values requires a description of the theoretical model used for the analysis of the measured thermal wave profiles and is discussed in the following section.

Next we present the result of Raman Thermography. Five representative room temperature experimental Raman spectra data were acquired under different excitation powers and shown in Fig. 4(a). Raman peak position was determined by fitting the peaks to a Gaussian profile, and as shown in Fig. 5(a), both D and G bands exhibit a linear shift to a smaller wavenumber with increasing incident power. This indicates that the local temperature of the PyC

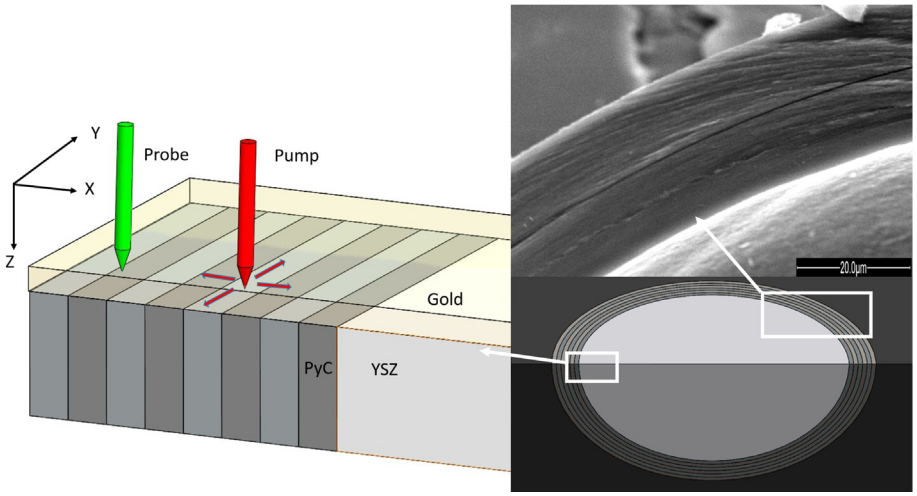

Fig. 1. Left: Planar representation of the textured PyC layer used in thermal transport model defined in Cartesian coordinate system. Top right: SEM image of the particle's cross section; Bottom right: 3D-rendering of the spherical particle showing that, locally, small sections can be considered to have planar geometry. (A colour version of this figure can be viewed online.)

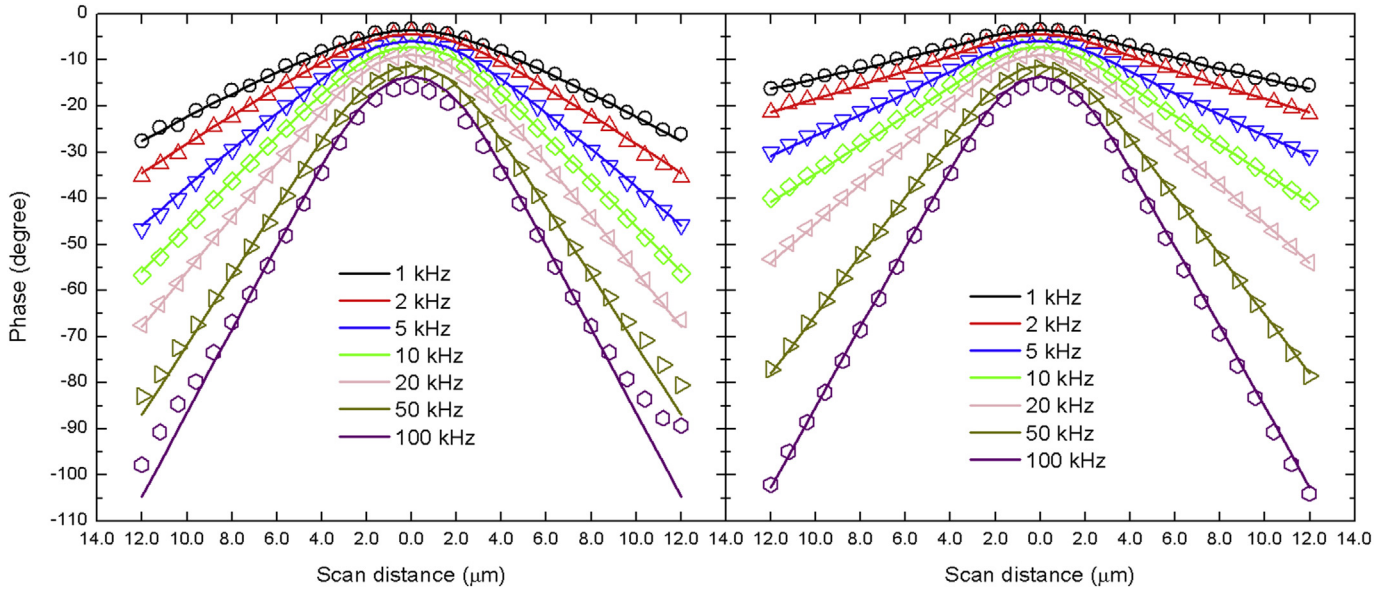

Fig. 2. Experimentally measured thermal wave phase profiles in PyC layer along the radial (left) and circumferential (right) directions of the spherical particle; symbols are experimental data and solid lines are model fits. (A colour version of this figure can be viewed online.)

increases under increasing laser power. Determination of the temperature on the surface of PyC required a calibration measurement that relates peak position to the temperature. For this, Raman spectra were collected as a function of temperature by placing the sample on a heated stage. Fig. 4(b) shows four representative experimental Raman spectra data and their corresponding Gaussian fits. In the temperature range from 296 to 364 K, the peaks shift towards smaller wavenumber with increasing temperature. Different fitting approaches are usually implemented to fit the Raman spectra that use Lorentzian or a combination of Gaussian and Lorentzian functions [51]. We need to stress here that using only Gaussian fitting may not provide the best result to extract additional details from the Raman spectra, but is preferred for area ratio. However, to study the peak position dispersion, our simple Gaussian fitting is justified since our interest is only in the linear position of the peak and linear fitting of χ_P and χ_T values eliminates any systematic error that arises. In fact, fitting with a combination of Breit-Wigner-Fano (BWF) line and Lorentzian functions were also conducted and this analysis revealed identical results.

4. Theoretical methods for data analysis

The model used for analysis of MTR profiles is based on the geometry depicted in Fig. 1. It captures a few-nanometer-thick gold film and the texture of the PyC layer with the basal plane along the circumferential direction. We neglect the curvature of the PyC coating because the thermal wave diffusion lengths are much smaller than the radius of curvature. The same diffusion length considerations allow us to neglect the influence of the YSZ core and the graphite matrix. A Cartesian coordinate system was locally defined where the *x* axis is parallel to the radial direction and *y* and *z* axes are in the circumferential direction. The *z* - *y* plane is parallel to the PyC basal planes, and the *z* axis corresponds to the depth

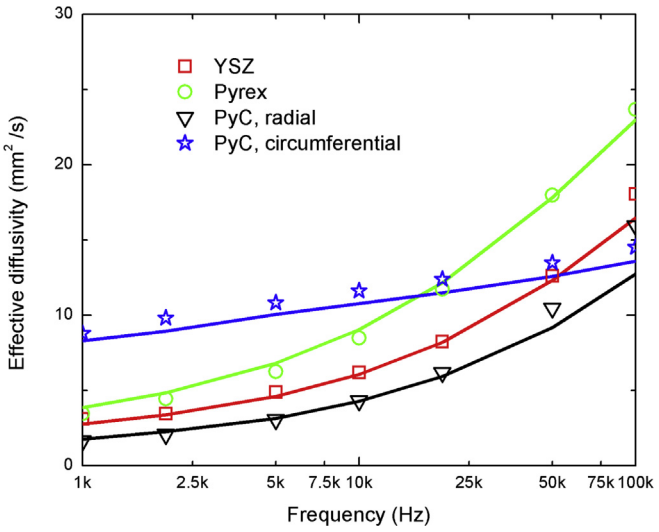

Fig. 3. Effective thermal diffusivity measured in different samples and along different directions over a broad frequency range, where symbols and solid lines are obtained from the analysis of the slopes in experimental and modeled phase profiles, respectively. (A colour version of this figure can be viewed online.)

direction (Fig. 1).

Based on the deposition conditions and symmetry arguments there are two independent conductivities, $k_{xx} = k_r$ and $k_{yy} = k_{zz} = k_c$. The subscripts r and c refer to radial and circumferential directions with respect to the spherical particle, respectively. The heat diffusion equation that accounts for metal layer in this coordinate system is defined as [52,53]:

$$\rho_f C_f \frac{\partial T_f}{\partial t} = k_f\left(\frac{\partial^2 T_f}{\partial x^2} + \frac{\partial^2 T_f}{\partial y^2} + \frac{\partial^2 T_f}{\partial z^2}\right) + P\delta^3\left(\vec{\mathbf{r}}\right)e^{i\omega t}\rho_s C_s \frac{\partial T_s}{\partial t} = \left(k_r \frac{\partial^2 T_s}{\partial x^2} + k_c \frac{\partial^2 T_s}{\partial y^2} + k_c \frac{\partial^2 T_s}{\partial z^2}\right) \quad (1)$$

where T is the temperature field, ρ is material density, C is specific heat, and P is the absorbed pump laser power. The subscript f refers to the metal film and s corresponds to the substrate material. The solution for T is convoluted with pump and probe profile to account for their finite spot sizes R_0. An analytical solution of Eq. (1) can be conveniently derived using an integral transform approach subject to the following 4 boundary conditions [37,54].

$$k_f \frac{\partial T_f}{\partial z}\Big|_{z=0} = 0$$
$$k_f \frac{\partial T_f}{\partial z}\Big|_{z=d} = k_c \frac{\partial T_s}{\partial z}\Big|_{z=d} = \frac{T_s - T_f}{R_{th}}\Big|_{z=d} \quad (2)$$
$$k_c \frac{\partial T_s}{\partial z}\Big|_{z=\infty} = 0$$

where d is the film thickness and R_{th} is the interface thermal resistance between film and substrate.

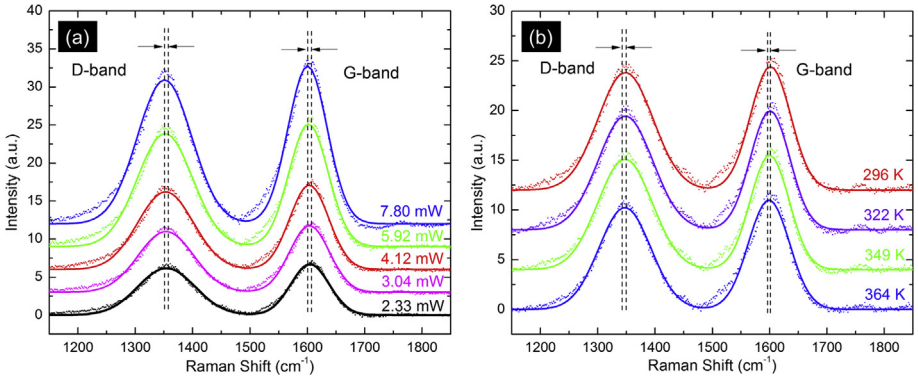

Fig. 4. Experimental data and Gaussian-fit Raman spectra of PyC sample. Experimental data are plotted by eliminating the base line and vertically shifted for clarity. (a) The Raman spectra of PyC under an incident laser power range of 2.33–7.80 mW. (b) Selected spectra from temperature calibration measurements. (A colour version of this figure can be viewed online.)

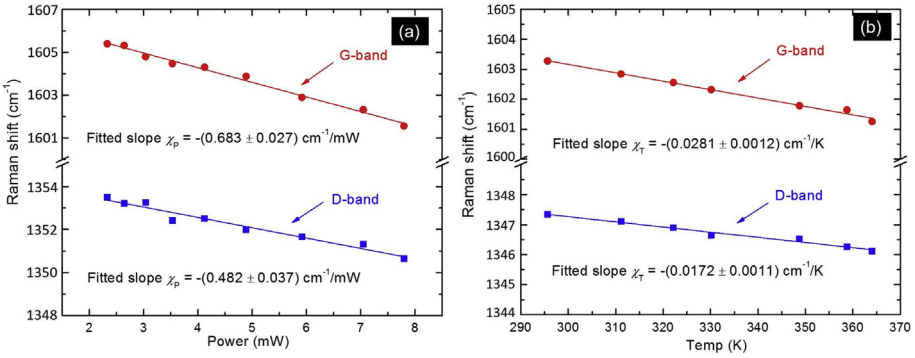

Fig. 5. (a) The Raman shift for both G and D modes as a function of laser power during the Raman experiments. Solid lines are fitting results for linear power coefficients χ_P. (b) The Raman shift for both G and D bands as a function of temperature in the calibration experiment. Solid lines are fitting results for linear temperature coefficients χ_T. (A colour version of this figure can be viewed online.)

To analyze the Raman results, we derived a separate analytical expression for the measured temperature on the surface of the PyC layer. In this case, the solution corresponds to a continuous excitation by the heater beam with a Gaussian profile of radius R_1 absorbed on the surface:

$$k_r\frac{\partial^2 T}{\partial^2 x}+k_c\left(\frac{\partial^2 T}{\partial^2 y}+\frac{\partial^2 T}{\partial^2 z}\right)+\frac{P}{2\pi R_1^2}e^{-\frac{x^2+y^2}{2R_1^2}}\delta(z)=0 \quad (3)$$

It can be shown that the temperature T measured by the second beam with a Gaussian profile of radius R_2 at the origin is:

$$T=\frac{P\sqrt{2\pi}}{2\pi^2}\frac{1}{k_c}\frac{1}{\sqrt{R_1^2+R_2^2}}K\left(\frac{k_c-k_r}{k_c}\right) \quad (4)$$

where $K(x)$ is the complete elliptic integral of the first kind. In our case of Raman Thermography $R_1 = R_2$.

5. Data analysis and discussion

5.1. Thermal conductivity from modulated thermoreflectance

To determine the unknown thermal conductivities, we followed an approach previously described in the literature [46]. Experimentally measured profiles were compared to the solution of diffusion equation defined by Eqs. (1) and (2). The unknown parameters were determined using a least square minimization procedure. First, we analyzed thermal wave profiles measured on the gold-coated Pyrex sample to determine conductivity of the gold film $k_f = 126$ W m^{-1} K^{-1}. In this analysis, in addition to isotropic thermal conductivity of Pyrex $k = 1.02$ W m^{-1} K^{-1}, specific heats and densities of both Pyrex and gold were considered as known and obtained from the literature or vendor (Table 1). Analysis of the Pyrex was also used to determine an additional phase lag introduced by the instrumentation under assumption that R_{th} between gold and Pyrex has negligible impact on the thermal wave profiles. This latter step is important for accurate determination of substrate conductivities larger than 5 W m^{-1} K^{-1}, as the impact of R_{th} cannot be accounted for properly from the analysis of the slopes alone and requires precise knowledge of phase lag at the origin [46].

Second, we analyzed thermal wave profiles obtained over YSZ to determine its conductivity and volumetric heat capacity ρC. Our values of $k = 1.73$ W m^{-1} K^{-1} and $\rho C = 2.47 \times 10^6$ J m^{-3} K^{-1} are comparable to the literature values of $k = 2.00$ W m^{-1} K^{-1} and vendor value of $\rho C = 2.74 \times 10^6$ J m^{-3} K^{-1}. Lower values in our measurement are attributed to the porosity of the YSZ particle.

To determine the anisotropic thermal conductivity of PyC, thermal wave phase profiles along the radial and circumferential directions were simultaneously fitted, where k_r, k_c, ρC, R_{th} and R_0 were used as fitting parameters. This analysis resulted in $\rho C = 1.15 \times 10^6$ J m^{-3} K^{-1} which is noticeably smaller than $\rho C = 1.54 \times 10^6$ J m^{-3} K^{-1} reported in the literature for 100% dense graphite at room temperature [56]. This suggests that the PyC layer is porous, which was expected under the current deposition conditions and consistent with electron microscopy image. Finally, the analysis revealed anisotropic thermal conductivity values of $k_r = 0.28$ W m^{-1} K^{-1} and $k_c = 11.5$ W m^{-1} K^{-1}, in agreement with our qualitative observation and confirmed textured nature of the PyC layer. The model also reveals that the interface thermal resistance between PyC and gold is $R_{th} = 2.09 \times 10^{-8}$ K m^2 W^{-1}.

Our fitting results revealed anisotropy ratio $k_c/k_r = 41$ confirming that the PyC layer exhibits ordered texture. Notably, our values for the conductivities in the radial and circumferential direction are significantly smaller than the cross-plane $k_\perp = 6.8$ W m^{-1} K^{-1} and in-plane $k_\parallel = 2000$ W m^{-1} K^{-1} for HOPG [1,16]. Nevertheless, our conductivity value in the circumferential direction is comparable to a range of 10–15 W m^{-1} K^{-1} reported for PyC layers prepared using similar approaches but with isotropic texture [33]. In general, the lower conductivity of PyC layers compared to graphite is attributed to the presence of disorder in the graphitic planes. This disorder is a result of the low temperature CVD deposition process and the absence of a high temperature annealing step. The latter is a critical step implemented during HOPG fabrication to achieve a complete graphitization of carbon. While measured ultralow value in the radial direction is comparable to the conductivity in few nm thick amorphous carbon layers, it has not been previously observed in as deposited textured graphitic carbons [57,58]. It should be noted that comparable values for anisotropic conductivity have been previously reported on reduced graphene oxide [59].

5.2. Effective conductivity from Raman thermography

Determination of the effective thermal conductivity based on RT measurement was done in 3 steps. First, the Raman peaks' position dependence on the excitation power was measured. Second, the Raman temperature calibration experiment was conducted, and the position dependence of the Raman peaks on temperature was determined. Third, the solution of the steady state heat conduction equation was applied to determine the effective thermal conductivity [22,27]. In the range of incident laser power (2.33–7.80 mW) and the temperature (296 K–364 K), the Raman peaks shift linearly depend on the laser power $\Delta\omega = \chi_P \Delta P$ and temperature $\Delta\omega = \chi_T \Delta T$, where χ_P, χ_T are the first-order laser power and temperature coefficients of the sample, P is the incident laser power, and T is the temperature [28]. For this opaque graphite, about 70% of the laser energy is absorbed in the graphite [60] and the absorbed energy is dissipated in the sample. The fitting results used to determine χ_T and χ_P for two bands are shown in Fig. 5(a) and (b) and summarized in Table 3. We use these parameters to determine the temperature rise per unit incident laser power using $\Delta\overline{T} = \chi_P \chi_T^{-1}$ (K mW^{-1}, Table 3).

Next, we compared the anisotropic conductivity values measured by MTR to the RT results. Applying conductivities measured by MTR listed in Table 2 and radius of $R_1 = R_2 = 0.48$ μm to Eq. (4), we estimate an average temperature rise per unit of incident power $\Delta\overline{T} = 25.02^{+2.84}_{-0.39}$ K mW^{-1}. This value is in close agreement with the temperature rise determined from the Raman analysis (Table 3) and provides additional validation for the MTR results.

Table 1
Properties of materials that were obtained from the literature.

Material	Conductivity, k (W m^{-1} K^{-1})	Density, ρ (kg m^{-3})	Specific heat, C (J kg^{-1} K^{-1})	Volumetric heat capacity, ρC (10^6 J m^{-3} K^{-1})
PyC [55]	~10 (cross-plane); ~2000 (in-plane)	1900	710	1.35
gold	Unknown	19,283	129	2.49
pyrex	1.02	2230	750	1.67
YSZ(5%)	2.00	6000	456	2.74

Table 2
Thermal conductivity fitting results.

Material	k_r (W m^{-1} K^{-1})	k_c (W m^{-1} K^{-1})	ρC (10^6 J m^{-3} K^{-1})
PyC	0.28 ± 0.07	11.5 ± 0.4	1.15 ± 0.02
YSZ	1.73 ± 0.10		2.47 ± 0.13
gold	126 ± 1		

5.3. Discussion

Considering the implemented deposition conditions, a textured PyC layer with large amount of disorder was expected. The layered texture of the coating has been confirmed by the measurement of anisotropic thermal conductivity. Additional details of the microstructure were determined from the analysis of Raman Spectra as described below. Raman spectra shown in Fig. 4 reveal both G and D bands. The G band is associated with an in-plane stretching motion of carbon atoms and is intrinsic to graphite [12]. The strong intensity of the D band associated with a breathing mode of carbon rings indicates the presence of disorder in the graphitic structure of the PyC layers [12,61] in agreement with our expectation based on deposition conditions.

Characterization of Raman spectra in carbon has been a subject of extensive research where position and width of the individual bands and the ratio of D to G band intensities have been used to determine grain size, texture, and ratio of sp^2 to sp^3 bonds [3,5,12]. We limited our analysis to extracting information that is useful to analyze measured thermal conductivity values. The Gaussian fitting used for thermography resulted in D and G bands located at 1350 cm^{-1} and 1600 cm^{-1}, peak width of 90 cm^{-1} and 64 cm^{-1}, respectively, and peak intensity ratio $A_D/A_G = 0.95$. Fitting using Lorentzian resulted in similar values. Qualitative analysis based on the work by Ferrari and Robertson suggests that the studied sample is nanocrystalline with an average grain size ranging 2–5 nm and contains small concentration of sp^3 bonds [12]. This corresponds to a transition region between two regimes for analytical expressions used to relate grain size to G and D peak intensity ratios. Large grain size regime expression has inverse dependence on grain size whereas the low grain size one has quadratic dependence [62]. Employing original Tuinstra and Koenig expression $A_D/A_G = C(\lambda)/L_a$, we estimate the grain size $L_a = 3.35$ nm, where A_D and A_G are the areas of D and G peaks, and $C(\lambda)$ is a parameter that depends on the wavelength of the laser λ [61]. If the expression for the small grain size limit $A_D/A_G = C'(\lambda)L_a^2$ is used then the grain size is $L_a = 2$ nm [63]. Applying the expression based on peak intensity ratio rather than area ratio, the Tuinstra and Koenig expression yielded a grain size of $L_a = 4.5$ nm.

The position and broadening of G peak at 1600 cm^{-1} is an indication that D′ peak appears at 1620 cm^{-1}. Recent works have indicated that the emergence of D′ peak is a result of confinement effects brought by the nanoscale grain size and activation of this band by disorder [64–66]. The width of the G peak can be used as a lower limit estimate of the grain size if the influence of D′ peak is neglected. We have $L_a = 1.0$ nm using $L_a = 4.6v/\Gamma_{FWHM}$ where v =13.3 cm^{-1} nmis the group velocity of the LO mode at the center of Brillouin zone [65,67]. The value is smaller than the one obtained from the peak ratio analysis and confirmed the calculations. Considering all these our estimated value for the grain size is 3.35 ± 1.3 nm.

Next, we present our analysis of the measured thermal conductivities within the framework of phonon-mediated thermal transport utilizing the microstructure information provided by Raman spectroscopy. We used the grain size determined from Raman to calculate the basal plane conductivity based on Klemens approach [68]. Based on this approach in-plane conductivity is 87.2 W m^{-1} K^{-1} at 3.35 nm grain size. To match the predicted conductivity to our experimental results an additional reduction due to point defect scattering needs to be included. This results in vacancy concentration around 2×10^{-2} per C atom which we found unphysical for our PyC sample. We attributed this to a failure of the single-band Debye approximation of phonon dispersion implemented in Klemens approach to accurately capture behavior of phonons across the broad range of phonon mean free paths [69].

Instead, we chose a model that considers the individual contributions from 3 acoustic branches in the phonon dispersion of graphite [70–72]. Our calculation of in-plane conductivity followed the approach described in Refs. [69] and [59]. In their implementation, phonons in each band are divided into two groups. High frequency phonons behavior is effectively described in 2D similar to Klemens [68] and low frequency modes behavior is 3D:

$$k^{2D} = \frac{\hbar^2}{4\pi^2 k_B T^2}\sum_s \frac{\omega_{c,s}}{v_s^{\perp}} \int_{\omega_{c,s}}^{\omega_{max,s}} \frac{\omega^3 \tau_s(\omega) exp(\hbar\omega/k_B T)}{[exp(\hbar\omega/k_B T) - 1]^2} d\omega k^{3D}$$

$$= \frac{\hbar^2}{4\pi^2 k_B T^2}\sum_s \frac{1}{v_s^{\perp}} \int_0^{\omega_{c,s}} \frac{\omega^4 \tau_s(\omega) exp(\hbar\omega/k_B T)}{[exp(\hbar\omega/k_B T) - 1]^2} d\omega \quad (5)$$

where $\hbar$ and k_B are Planks and Boltzmann constants, ω is phonon frequency, s denotes one of the longitudinal (LA), in-plane transverse (TA), and out of plane transverse (ZA) acoustic modes. $v_s^{\perp}$ is out-of-plane phonon group velocity of branch s, and $\tau_s(\omega)$ is the branch and frequency dependent phonon relaxation time. $\omega_{c,s}$ is the cut-off frequency that separates 2D and 3D phonons and is related to the maximum frequency of the corresponding phonon mode propagating normal to the basal plane [69]. $\omega_{max,s}$ is the maximum frequency of each phonon branch. In our analysis we employed linear dispersion and only considered three phonon scattering processes: Umklapp scattering τ_i^{-1}, grain boundary scattering τ_g^{-1}, and point defect scattering τ_p^{-1}. Total phonon relaxation time was calculated using Matthiessen's rule: $\tau^{-1} = \tau_i^{-1} + \tau_g^{-1} + \tau_p^{-1}$, where $\tau_g^{-1} = v_s/L$, $\tau_i^{-1} = \gamma_s^2 k_B T \omega^2/(M v_s^2 \omega_{max,s})$, and v_s is in-plane group velocity. $\gamma_{LA} = 2$, $\gamma_{TA} = 1$ and $\gamma_{ZA} = -1.5$. In graphite most point defects are vacancies, and their effect on relaxation time is $\tau_p^{-1} = 2\pi\omega^3\Gamma/\omega_{max,s}^2$, where $\Gamma = \sum c(\Delta M/M)^2$ is a scattering strength, c is the concentration of defects per carbon atom, and ΔM is the mass difference between the defect and the carbon atom, M. Vacancy in graphite has $\left(\frac{\Delta M}{M}\right) = 3$ [68].

Table 3
Results of Raman thermometry.

	D-band	G-band
Power coefficient, χ_P (cm^{-1} mW^{-1})	−0.48 ± 0.4	−0.683 ± 0.027
Temperature coefficient, χ_T (cm^{-1} K^{-1})	−0.0172 ± 0.001	−0.028 ± 0.001
$\Delta\overline{T}$ (K mW^{-1})	28.0 ± 2.8	24.3 ± 1.4

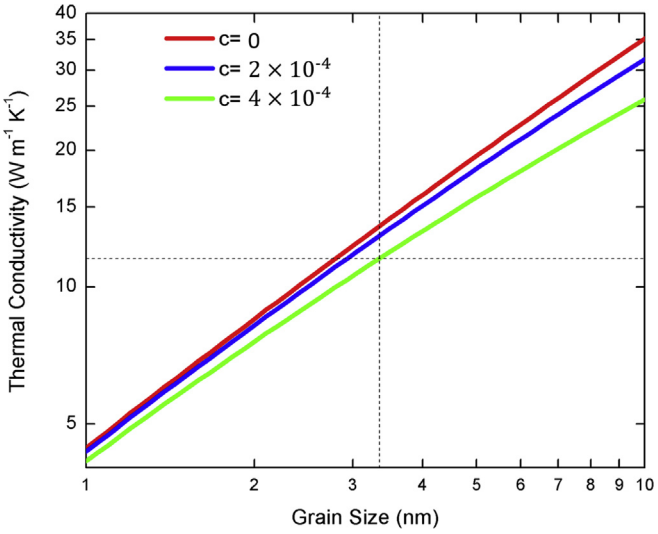

Fig. 6. Calculated in-plane thermal conductivity for a range of grain sizes and vacancy concentrations. Dashed lines correspond to the experimentally measured values of circumferential conductivity and grain size using MTR and Raman Spectroscopy, respectively. (A colour version of this figure can be viewed online.)

Fig. 6 represents in-plane conductivity calculated using Eq. (5) as a function of grain size and 3 different vacancy concentrations. We see that the range for calculated conductivity corresponding to 2–5 nm grain size captures our measured conductivity value. Specifically, a grain size of $L_a = 3.35$ nm and neglecting point defects, the calculated conductivity is 14.4 W m^{-1} K^{-1}, higher than our experimental value of 11.5 W m^{-1} K^{-1}. The model conductivity for this grain size matches our result when point defect scattering strength equals $\Gamma = 3.6 \times 10^{-3}$. If all this scattering is attributed to vacancies their concentration would be per carbon atom $c = 4 \times 10^{-4}$. It is also possible that some atomic hydrogen in the form of C–H bonds are present in the PyC layer. While we were not able to identify the exact nature of the point defects and only used vacancy as an example, we can infer their presence and contribution to the phonon lifetime based on the analysis of Raman spectra (Fig. 4).

Quantifying the G-band's broadening to determine phonon lifetime is complicated by the emergence of the D′ band. G-band normally located at 1580 cm^{-1} is associated with the LO optical mode and its broadening is attributed to disorder introduced by small grains and point defects [63,73–76]. The same disorder activates the TO mode which corresponds to D′ band located around 1620 cm^{-1}. The fact that the 1600 cm^{-1} band appears as a single peak is an indication of large broadening of both G and D′ bands originating from factors other than just nanocrystalline grain size. This further justifies the use of point defect scattering term in our thermal transport model. In principle it should be possible to systematically analyze the Raman spectra to isolate the contribution of various microstructure features and use those as input parameters for thermal transport mode, but was not possible in this work as it would require analysis of a larger set of experimental samples.

Previous discussion was based on the assumption that measured conductivity in the circumferential direction corresponds to the basal plane conductivity. This would be the case if a perfectly textured structure existed where the graphitic layers were aligned along the circumferential direction. In the case of a tilt in the basal plane of graphite, the actual basal plane conductivity would be higher. Furthermore, previous studies have shown that the width of the D peak is also an indication of structure disorders, and is sensitive to in-plane defects [77]. Our measured D peak full width at half maximum of 90 cm^{-1} falls into the range corresponding to smooth laminar PyC with turbulence in the basal plane [5]. This supports our previous conclusion that the PyC layer is textured and also provides a reason for low anisotropy ratio. Despite this, we anticipate that for measured conductivity anisotropy ratio of 41 these two effects are small and don't significantly affect the analysis presented in the previous paragraphs.

Lastly, we discuss the low conductivity along the radial direction. The measured values of $k = 0.28$ W m^{-1} K^{-1} is comparable to the lowest reported value for amorphous carbon and smaller than $k = 0.8$ W m^{-1} K^{-1}, calculated minimum thermal conductivity for diamond [58,78]. We estimated the minimum cross-plane thermal conductivity for graphite using the expression of minimum conductivity [58]:

$$\kappa_{min} = \frac{\hbar^2}{6\pi k_B T^2} \sum_s \int_0^{\omega_{c,s}} \frac{\omega^3 \exp(\hbar\omega/k_B T)}{v_s^{\perp} [\exp(\hbar\omega/k_B T) - 1]^2} d\omega \tag{6}$$

and find k_{min} to be 0.38 W m^{-1}K^{-1}. Our measured conductivity is slightly lower than these minimum bulk conductivity values and is attributed to the delamination and air pockets between layers (Fig. 1), similar to the previous observation in textured reduced graphene oxide [59].

We conclude the discussion by emphasizing that the analysis presented above can be further expanded and used to optimize the deposition condition and subsequent thermal treatment to develop a microstructure with desired anisotropic thermal properties by tailoring grain size and texture quality [3]. Current low temperature deposition conditions were chosen to obtain lowest conductivity in the radial direction. For applications as a directional heat spreader, a very large thermal anisotropy would be desired and would require processing at higher temperatures. A combination of deposition conditions, thermal conductivity measurements and Raman characterization offers an opportunity to optimize thermal property of PyC coating and is an attractive topic for future work.

6. Conclusions

A moderately textured pyrolytic carbon layer with the basal plane aligned parallel to the circumferential direction was deposited on a spherical YSZ particle. The anisotropic thermal transport properties of the PyC layer were investigated using a laser-based modulated thermoreflectance method at room temperature. An analytical solution of the heat diffusion equation was developed and used to analyze measured thermal wave profiles. We found that the thermal conductivity in the circumferential and radial direction are 11.53 W m^{-1} K^{-1} and 0.28 W m^{-1} K^{-1}, respectively, which are substantially smaller than the basal and cross plane conductivity of HOPG. A separate Raman experiment was conducted to validate these results. Microstructural characterization based on Raman spectroscopy revealed a graphitic structure with a high degree of disorder and a grain size of a few nanometers. Phonon-mediated thermal transport formalism based on the defect microstructure obtained from Raman spectroscopy was applied to estimate thermal conductivity in the basal plane. We found an agreement between measured circumferential conductivity and model calculation. We also hypothesize that porosity and debonding between graphitic planes are responsible for additional reduction in thermal conductivity in the radial direction beyond the theoretical minimum limit of the graphite's cross-plane conductivity. The anisotropic thermal properties and ultralow conductivity normal to the surface of the substrate offers attractive opportunities for heat management in energy and electronics applications.

Acknowledgements

Y. W. and M. K. acknowledge the support from NRC Faculty Development Program (NRC-HQ-13-G-38-0044). E. P. L., I. O. U. and M. F. B. acknowledge the support from LANL LDRD Program (20150058DR). P. Y. and X. W. acknowledge the support from National Science Foundation (CBET1235852, CMMI1264399), and Department of Energy (DENE0000671, DE-EE0007686). Authors also acknowledge the assistance from Thomas Martin in preparation of the manuscript. Approved for release under LA-UR-17-25392.

References

[1] A.A. Balandin, Thermal properties of graphene and nanostructured carbon materials, Nat. Mater. 10 (8) (2011) 569–581.
[2] G.A. Slack, Anisotropic thermal conductivity of pyrolytic graphite, Phys. Rev. 127 (3) (1962) 694–701.
[3] E. Lopez-Honorato, P. Meadows, P. Xiao, Fluidized bed chemical vapor deposition of pyrolytic carbon - I. Effect of deposition conditions on microstructure, Carbon 47 (2) (2009) 396–410.
[4] P. Dupel, X. Bourrat, R. Pailler, Structure of pyrocarbon infiltrated by pulse-CVI, Carbon 33 (9) (1995) 1193–1204.
[5] J. Vallerot, X. Bourrat, A. Mouchon, G. Chollon, Quantitative structural and textural assessment of laminar pyrocarbons through Raman spectroscopy, electron diffraction and few other techniques, Carbon 44 (9) (2006) 1833–1844.
[6] E. Bortchagovsky, B. Reznik, D. Gerthsen, A. Pfrang, T. Schimmel, Optical properties of pyrolytic carbon deposits deduced from measurements of the extinction angle by polarized light microscopy, Carbon 41 (12) (2003) 2430–2433.
[7] P. Meadows, E. Lopez-Honorato, P. Xiao, Fluidized bed chemical vapor deposition of pyrolytic carbon - II. Effect of deposition conditions on anisotropy, Carbon 47 (1) (2009) 251–262.
[8] A.A. Campbell, K.B. Campbell, G.S. Was, Anisotropy analysis of ultra-fine grain graphite and pyrolytic carbon, Carbon 60 (2013) 410–420.
[9] H.O. Pierson, Handbook of Carbon, Graphite, Diamonds and Fullerenes Processing, Properties and Applications, first ed., Noyes Publications, N.J., 1993.
[10] M. Wang, Q. Kang, N. Pan, Thermal conductivity enhancement of carbon fiber composites, Appl. Therm. Eng. 29 (2–3) (2009) 418–421.
[11] S. Zhou, Y. Zhu, H. Du, B. Li, F. Kang, Preparation of oriented graphite/polymer composite sheets with high thermal conductivities by tape casting, New Carbon Mater 27 (4) (2012) 241–249.
[12] A. Ferrari, J. Robertson, Interpretation of Raman spectra of disordered and amorphous carbon, Phys. Rev. B 61 (20) (2000) 14095–14107.
[13] H. Nickel, Pyrocabon and its application to reactor technology, J. Vac. Sci. Technol. 11 (4) (1974) 687–694.
[14] D. Petti, J. Maki, J. Hunn, P. Pappano, C. Barnes, J. Saurwein, et al., The DOE advanced gas reactor fuel development and qualification Program, JOM 62 (9) (2010) 62–66.
[15] D.P. Harmon, C.B. Scott, Properties influencing high-temperature gas-cooled reactor coated fuel particle performance, Nucl. Technol. 35 (2) (1977) 343–352.
[16] R. Taylor, The thermal conductivity of pyrolytic graphite, Philos. Mag. 13 (121) (1966) 157–166.
[17] J.R. Lamarsh, A.J. Baratta, Introduction to Nuclear Engineering, third ed., Pearson, New Jersey, 2001.
[18] D.A. Petti, P.A. Demkowicz, J.T. Maki, R.R. Hobbins, TRISO-coated Particle Fuel Performance, Reference Module in Materials Science and Materials Engineering, Comprehensive Nuclear Materials, First ed., Elsevier Science, 2012, pp. 152–213.
[19] R. Matsumoto, Y. Hoshina, N. Akuzawa, Thermoelectric properties and electrical transport of graphite intercalation compounds, Mater. Trans. 50 (7) (2009) 1607–1611.
[20] G.E. Jellison Jr., J.D. Hunn, R.A. Lowden, Optical characterization of tristructural isotropic fuel particle cross-sections using generalized ellipsometry, J. Nucl. Mater. 352 (1–3) (2006) 6–12.
[21] D. Rochais, H. Le Houedec, F. Enguehard, J. Jumel, F. Lepoutre, Microscale thermal characterization at temperatures up to 1000 deg C by photoreflectance microscopy Application to the characterization of carbon fibres, J. Phys. D Appl. Phys. 38 (10) (2005) 1498–1503.
[22] C. Faugeras, B. Faugeras, M. Orlita, M. Potemski, R. Nair, A. Geim, Thermal conductivity of graphene in corbino membrane geometry, Acs Nano 4 (4) (2010) 1889–1892.
[23] H. Malekpour, K.H. Chang, J.C. Chen, C.Y. Lu, D.L. Nika, K.S. Novoselov, et al., Thermal conductivity of graphene laminate, Nano Lett. 14 (9) (2014) 5155–5161.
[24] W.D. Swank, W.E. Windes, Specimen Size Effects in the Determination of Nuclear Grade Graphite Thermal Diffusivity, ASTM Symposium on Graphite Testing for Nuclear Applications: the Significance of Test Specimen Volume and Geometry and the Statistical Significance of Test Specimen Population, 2014, pp. 186–198. Seattle, WA.
[25] C.H. Wu, J.P. Bonal, B. Thiele, Thermal conductivity changes in graphites and carbon/carbon fiber materials induced by low neutron damages, J. Nucl. Mater. 212–215 (1994) 1168–1173. Part B.
[26] L.L. Snead, T.D. Burchell, Thermal conductivity degradation of graphites due to nuetron irradiation at low temperature, J. Nucl. Mater. 224 (3) (1995) 222–229.
[27] C. Li, S. Xu, Y. Yue, B. Yang, X. Wang, Thermal characterization of carbon nanotube fiber by time-domain differential Raman, Carbon 103 (2016) 101–108.
[28] P. Yuan, C. Li, S. Xu, J. Liu, X. Wang, Interfacial thermal conductance between few to tens of layered-MoS_2 and c-Si: effect of MoS2 thickness, Acta Mater. 122 (2017) 152–165.
[29] E. Lopez-Honorato, P. Meadows, R. Shatwell, P. Xiao, Characterization of the anisotropy of pyrolytic carbon by Raman spectroscopy, Carbon 48 (3) (2010) 881–890.
[30] C. Chiritescu, D. Cahill, N. Nguyen, D. Johnson, A. Bodapati, P. Keblinski, et al., Ultralow thermal conductivity in disordered, layered WSe2 crystals, Science 315 (5810) (2007) 351–353.
[31] X. Zheng, D.G. Cahill, J.C. Zhao, Thermal conductivity imaging of thermal barrier coatings, Adv. Eng. Mater. 7 (7) (2005) 622–626.
[32] W. Capinski, H. Maris, Improved apparatus for picosecond pump-and-probe optical measurements, Rev. Sci. Instrum. 67 (8) (1996) 2720–2726.
[33] D. Rochais, G. Le Meur, V. Basini, G. Domingues, Microscopic thermal characterization of HTR particle layers, Nucl. Eng. Des. 238 (11) (2008) 3047–3059.
[34] J. Hartmann, P. Voigt, M. Reichling, Measuring local thermal conductivity in polycrystalline diamond with a high resolution photothermal microscope, J. Appl. Phys. 81 (7) (1997) 2966–2972.
[35] C. Wei, X. Zheng, D. Cahill, J. Zhao, Invited Article: micron resolution spatially resolved measurement of heat capacity using dual-frequency time-domain thermoreflectance, Rev. Sci. Instrum. 84 (7) (2013), 071301.
[36] J. Feser, J. Liu, D. Cahill, Pump-probe measurements of the thermal conductivity tensor for materials lacking in-plane symmetry, Rev. Sci. Instrum. 85 (10) (2014), 104903.
[37] D. Hurley, K. Telschow, Simultaneous microscopic imaging of elastic and thermal anisotropy, Phys. Rev. B 71 (24) (2005), 241410.
[38] B. Li, L. Pottier, J. Roger, D. Fournier, K. Watari, K. Hirao, Measuring the anisotropic thermal diffusivity of silicon nitride grains by thermoreflectance microscopy, J. Eur. Ceram. Soc. 19 (8) (1999) 1631–1639.
[39] A. Rosencwaig, J. Opsal, W. Smith, D. Willenborg, Detection of thermal waves through optical reflectance, Appl. Phys. Lett. 46 (11) (1985) 1013–1015.
[40] J. Pakarinen, M. Khafizov, L. He, C. Wetteland, J. Gan, A.T. Nelson, et al., Microstructure changes and thermal conductivity reduction in UO2 following 3.9 MeV He 2+ ion irradiation, J. Nucl. Mater. 454 (1–3) (2014) 283–289.
[41] R. Cheaito, C.S. Gorham, A. Misra, K. Hattar, P.E. Hopkins, Thermal conductivity measurements via time-domain thermoreflectance for the characterization of radiation induced damage, J. Mater. Res. 30 (9) (2015) 1403–1412.
[42] V.S. Chauhan, M.F. Riyad, X. Du, C. Wei, B. Tyburska-Püschel, J.-C. Zhao, et al., Thermal conductivity degradation and microstructural damage characterization in low-dose ion beam-irradiated 3C-SiC, Metall. Trans. E 4 (2017) 61–69.
[43] M. Khafizov, V. Chauhan, Y. Wang, F. Riyad, N. Hang, D. Hurley, Investigation of thermal transport in composites and ion beam irradiated materials for nuclear energy applications, J. Mater. Res. 32 (1) (2016) 204–216.
[44] I. Usov, M. Beaux II, D.R. Vodnik, G. King, K. Hubbard, B. Bennet, et al., Pyrolytic Carbon Coatings on Oxide and Carbide Microspheres, Materials Science & Technology 2016 Meeting, Salt Lake City, UT, USA, 2016.
[45] M.F. Beaux II, D.R. Vodnik, R.J. Peterson, B.L. Bennett, K.C. Henderson, B.M. Patterson et al., Pyrolytic carbon coating effects on oxide and carbide kernels for nuclear fuel applications, J. Nucl. Mater. (to be submitted).
[46] D. Hurley, R. Schley, M. Khafizov, B. Wendt, Local measurement of thermal conductivity and diffusivity, Rev. Sci. Instrum. 86 (12) (2015), 123901.
[47] G. Jellison, J. Hunn, H. Lee, Measurement of optical functions of highly oriented pyrolytic graphite in the visible, Phys. Rev. B 76 (8) (2007), 085125.
[48] E. Lopez-Honorato, H. Zhang, R. Shatwell, P. Guillermier, D. Manara, P. Xiao, et al., Analysis of the anisotropy, stoichiometry and polytypes in pyrolytic carbon and silicon carbide coatings, J. Nucl. Mater. 432 (1–3) (2013) 334–340.
[49] A. Maznev, J. Hartmann, M. Reichlling, Thermal-wave propagation in thin-films on substrates, J. Appl. Phys. 78 (9) (1995) 5266–5269.
[50] J. Hartmann, P. Voigt, M. Reichling, E. Matthias, Photothermal measurement of thermal anisotropy in pyrolytic graphite, Appl. Phys. B Laser Optic. 62 (5) (1996) 493–497.
[51] A. Sadezky, H. Muckenhuber, H. Grothe, R. Niessner, U. Pöschl, Raman microspectroscopy of soot and related carbonaceous materials: spectral analysis and structural information, Carbon 43 (8) (2005) 1731–1742.
[52] M. Iravani, M. Nikoonahad, Photothermal waves in anisotropic media, J. Appl. Phys. 62 (10) (1987) 4065–4071.
[53] D. Hurley, M. Fig, Parametric study of thermal interface resistance using laser-based thermal wave imaging, J. Appl. Phys. 104 (12) (2008), 123703.
[54] M. Khafizov, D. Hurley, Measurement of thermal transport using time-resolved thermal wave microscopy, J. Appl. Phys. 110 (8) (2011) 083525.
[55] V. Basini, F. Charollais, New Techniques Dedicated to the Characterization of Future Nuclear Fuels, Hot Laboratories and Remote Handling, National Institute for Nuclear Science and Technology - INSTN, France, 2003, p. 260.

[56] E. Pop, V. Varshney, A. Roy, Thermal properties of graphene: fundamentals and applications, MRS Bull. 37 (12) (2012) 1273–1281.
[57] A. Balandin, M. Shamsa, W. Liu, C. Casiraghi, A. Ferrari, Thermal conductivity of ultrathin tetrahedral amorphous carbon films, Appl. Phys. Lett. 93 (4) (2008), 043115.
[58] A. Bullen, K. O'Hara, D. Cahill, O. Monteiro, A. von Keudell, Thermal conductivity of amorphous carbon thin films, J. Appl. Phys. 88 (11) (2000) 6317–6320.
[59] J. Renteria, S. Ramirez, H. Malekpour, B. Alonso, A. Centeno, A. Zurutuza, et al., Strongly anisotropic thermal conductivity of free-standing reduced graphene oxide films annealed at high temperature, Adv. Funct. Mater. 25 (29) (2015) 4664–4672.
[60] B.J. Stagg, T.T. Charalampopoulos, Refractive indices of pyrolytic graphite, amorphous carbon, and flame soot in the temperature range 25° to 600°C, Combust. Flame 94 (4) (1993) 381–396.
[61] F. Tuinstra, J. Koenig, Raman spectrum of graphite, J. Chem. Phys. 53 (3) (1970) 1126.
[62] A. Ferrari, D. Basko, Raman spectroscopy as a versatile tool for studying the properties of graphene, Nat. Nanotechnol. 8 (4) (2013) 235–246.
[63] P. Mallet-Ladeira, P. Puech, C. Toulouse, M. Cazayous, N. Ratel-Ramond, P. Weisbecker, et al., A Raman study to obtain crystallite size of carbon materials: a better alternative to the Tuinstra-Koenig law, Carbon 80 (2014) 629–639.
[64] L. Cancado, A. Jorio, E. Ferreira, F. Stavale, C. Achete, R. Capaz, et al., Quantifying defects in graphene via Raman spectroscopy at different excitation energies, Nano Lett. 11 (8) (2011) 3190–3196.
[65] P. Puech, J. Plewa, P. Mallet-Ladeira, M. Monthioux, Spatial confinement model applied to phonons in disordered graphene-based carbons, Carbon 105 (2016) 275–281.
[66] E. Ferreira, M. Moutinho, F. Stavale, M. Lucchese, R. Capaz, C. Achete, et al., Evolution of the Raman spectra from single-, few-, and many-layer graphene with increasing disorder, Phys. Rev. B 82 (12) (2010) 125429.
[67] M. Lazzeri, S. Piscanec, F. Mauri, A. Ferrari, J. Robertson, Phonon linewidths and electron-phonon coupling in graphite and nanotubes, Phys. Rev. B 73 (15) (2006) 155426.
[68] P. Klemens, D. Pedraza, Thermal-conductivity of graphite in the basal-plane, Carbon 32 (4) (1994) 735–741.
[69] D. Nika, A. Askerov, A. Balandin, Anomalous size dependence of the thermal conductivity of graphene ribbons, Nano Lett. 12 (6) (2012) 3238–3244.
[70] S. Reich, C. Thomsen, H. Requardt, P. Ordejón, Phonon dispersion in graphite, Phys. Rev. Lett. 92 (7) (2004), 075501.
[71] M. Mohr, J. Maultzsch, E. Dobardžić, S. Reich, I. Milošević, M. Damnjanović, et al., Phonon dispersion of graphite by inelastic x-ray scattering, Phys. Rev. B 76 (3) (2007), 035439.
[72] R. Nicklow, N. Wakabayashi, H.G. Smith, Lattice dynamics of pyrolytic graphite, Phys. Rev. B 5 (12) (1972) 4962.
[73] K. Ishioka, M. Hase, K. Ushida, M. Kitajima, Phonon dynamics in ion-irradiated graphite and GaAs, Appl. Surf. Sci. 197 (2002) 726–729.
[74] A. Aitkaliyeva, M.S. Martin, T.A. Harriman, D.S. Hildebrand, D.A. Lucca, J. Wang, et al., Radiation effects on the D to G Raman intensities of carbon nanotubes, Phys. Rev. B 89 (23) (2014), 235437.
[75] D. Abdula, K. Nguyen, K. Kang, S. Fong, T. Ozel, D. Cahill, et al., Influence of defects and doping on optical phonon lifetime and Raman linewidth in carbon nanotubes, Phys. Rev. B 83 (20) (2011), 205419.
[76] A. Alofi, G. Srivastava, Thermal conductivity of graphene and graphite, Phys. Rev. B 87 (11) (2013), 115421.
[77] X. Bourrat, Pyrocarbon Performances and Characterization, World Conference on Carbon, Biarritz, France, 2009.
[78] C. Morath, H. Maris, J. Coumo, D. Pappas, A. Grill, V. Patel, et al., Picosecond optical studies of amorphous diamond and diamondlike carbon: thermal conductivity and longitudinal sound velocity, J. Appl. Phys. 76 (5) (1994) 2636–2640.